Digest Journal of Nanomaterials and Biostructures Vol. 20, No. 4, October-December 2025, p. 1519-1537

Investigation of the detection mechanism and performance of gallium oxide ultraviolet photodetector by numerical analysis

W. C. Huang [a], J. X. Xu [a,*], Z. Liu [a]
[a] *School of Integrated Circuits, Guangdong University of Technology, Guangzhou 510006, China*

Gallium oxide (Ga_2O_3) photodetector is regarded as a promising candidate for ultraviolet detection, owing to its rapid response characteristics and high responsivity. Specifically, the metal-semiconductor-metal (MSM) structured Ga_2O_3 photodetector offers the benefits of simple fabrication and fast response speed. In this study, the effects of illumination wavelength and intensity, absorber thickness and doping concentration, and ambient temperature on the detection performances of Au/Ga_2O_3/Au photodetector were investigated by a numerical analysis method. The calculated results demonstrate that the Ga_2O_3 photodetector can efficiently and selectively absorb solar-blind ultraviolet light because of the ultra-wide bandgap of the Ga_2O_3 layer. The Ga_2O_3 photodetector exhibited a linear response to the illumination intensity at 254 nm. The increases in the thickness and electron concentration of the Ga_2O_3 layer and a decrease in ambient temperature enhance the solar-blind ultraviolet detection performances of the metal-semiconductor-metal structure Ga_2O_3 device. The calculated detection performances can be explained from the processes of absorption of ultraviolet light, formation of photo-generated carriers, and transport of carriers to the metal electrode using the band diagram of the device. The carrier recombination and the role of the barrier at the metal/Ga_2O_3 interface were considered in the detection mechanism analysis. This work presents insight into the operational mechanisms of Ga_2O_3 photodetectors and the effective ways to improve their performance by appropriate device parameters and working conditions.

(Received September 15, 2025; Accepted December 12, 2025)

Keywords: Solar-blind ultraviolet photodetector, Gallium oxide, Metal-semiconductor-metal structure, Absorption, Recombination

1. Introduction

Solar-blind ultraviolet photodetectors are specifically designed to detect the solar-blind ultraviolet light, which corresponds to wavelengths between 200 and 280 nm. The solar radiation at these wavelengths is almost completely absorbed by the ozone layer. Consequently, solar-blind ultraviolet photodetectors operate with inherent immunity to solar interference, making them crucial for applications including chemical analysis, environmental monitoring, space exploration, and biological sensing [1–4]. Wide-bandgap materials, such as gallium nitride (GaN), zinc oxide

* Corresponding author: xujiaxiong@gdut.edu.cn
https://doi.org/10.15251/DJNB.2025.204.1519

(ZnO), aluminum gallium nitride (AlGaN), and gallium oxide (Ga_2O_3), enable efficient absorption of ultraviolet light and generation of photocurrent [5–8]. Among these materials, the deep-ultraviolet transparent direct bandgap semiconductor Ga_2O_3 offers several notable advantages [9–11]. Ga_2O_3 has a wide-bandgap of around 4.8 eV, which aligns well with the solar-blind ultraviolet region. Ga_2O_3 exhibits an exceptionally high breakdown electric field, making it promising for use in high-frequency, high-temperature, and high-power devices. These characteristics ensure stable device performance across a variety of operating environments.

Currently, the device structures employed for Ga_2O_3 ultraviolet photodetectors include metal-semiconductor-metal (MSM), Schottky junction, heterojunction, and field-effect transistor (FET) [12–16]. Among them, the MSM structure has a simple fabrication process, low manufacturing cost, and fast response speed. Kuang et al. fabricated Ga_2O_3 photodetectors by molecular beam epitaxy, achieving a photodetector responsivity of up to 167 A/W. However, the device exhibited a significant dark current, which hindered further enhancement of its overall performance [17]. Meanwhile, Huang et al. investigated a MSM-structured photodetector based on a β-Ga_2O_3 layer deposited via thermal atomic layer deposition. While this device demonstrated faster response speed, its responsivity remained relatively low [18].

To gain deeper insights into the operational mechanisms and performance-determining factors of Ga_2O_3 photodetectors, numerical simulation has become an indispensable tool for device analysis and optimization. However, few studies have been reported on the numerical modeling of Ga_2O_3 photodetectors [19,20]. Xu et al. modeled a Ga_2O_3/diamond heterostructure photodiode, evaluating cutoff wavelength, electric field distribution, gain, and responsivity [19]. Zhang et al. designed an Al/Al_2O_3/Ga_2O_3 metal-insulator-semiconductor photodetector featuring enhanced ultralow dark current. Through optimization of electrode dimensions, the device's responsivity was further improved [20]. While previous simulation studies have advanced the understanding of Ga_2O_3 photodetectors to some extent, a comprehensive investigation of critical parameters, including the doping concentration of the active layer and operating temperature, is required to elucidate the detection mechanisms and performance characteristics of Ga_2O_3 photodetectors. However, existing literature has not adequately addressed these parameter-dependent effects.

In this study, the performance of MSM-structured Au/Ga_2O_3/Au photodetectors was thoroughly analyzed through numerical simulation, enabling the role of physical parameters and clarifying the underlying conduction mechanisms. Au electrode offers significant advantages of its superior electrical conductivity and low resistivity, which ensure efficient current transport and minimal energy dissipation. The numerical analysis focused on the thickness-dependent light absorption dynamics, doping-regulated carrier transport behavior, and temperature-activated processes governing device performances. This work enhances the fundamental understanding of carrier transport mechanisms in Ga_2O_3 photodetectors while offering technical guidelines for the design and fabrication of solar-blind ultraviolet detection systems.

2. Calculated methodology

The numerical calculations of the Ga_2O_3 photodetector were performed using AFors-Het software [21]. First, the device structure was constructed as illustrated in Fig. 1. The photodetector adopted an Au/Ga_2O_3/Au stack configuration, with Ga_2O_3 serving as the semiconductor absorber

layer and the metal layers acting as the front and back electrodes. The incident light was directed toward the device from the front electrode side. The material parameters for Ga_2O_3 and the Au layers, used in the calculations, were obtained from Refs. [22–24] and are summarized in Tables 1 and 2.

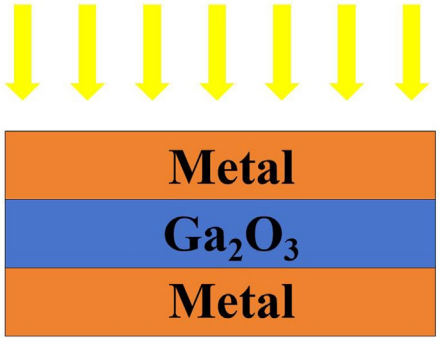

Fig. 1. Schematic diagram of the MSM-structured Ga_2O_3 photodetector. MSM, metal-semiconductor-metal; Ga_2O_3, gallium oxide.

Table 1. Material parameters of Ga_2O_3 used for numerical calculation.

Parameters	Value	Unit
Thickness	200	nm
Dielectric constant	10.2	–
Electron affinity	4.0	eV
Bandgap energy	4.8	eV
Effective conduction band density	3.72×10^{19}	cm^{-3}
Effective valence band density	1.16×10^{19}	cm^{-3}
Electron mobility	300	$cm^2 \cdot V^{-1} \cdot s^{-1}$
Hole mobility	1.3	$cm^2 \cdot V^{-1} \cdot s^{-1}$
Acceptor doping concentration	0	cm^{-3}
Donor doping concentration	1×10^{17}	cm^{-3}

Table 2. Material parameters of metal contacts used for numerical calculation.

Parameters	Value	Unit
Thickness	10	nm
Work function	5.1	eV

The performances of the Ga_2O_3 photodetector were obtained based on a drift-diffusion model. The Poisson equation, as well as the continuity and transport equations for electrons and holes, was numerically solved. This enables a comprehensive description of the internal physical processes within the device, including electric potential distribution, carrier generation, transport, and recombination [21, 25]. The photon absorption process within the material was modeled using the Lambert-Beer law, while also taking into account the effects of multiple internal reflections to better approximate real-world illumination conditions. Additionally, the integration of various recombination models, such as band-to-band recombination, Shockley-Read-Hall (SRH) recombination, and Auger recombination, allowed for a comprehensive representation of carrier recombination pathways.

The ultraviolet-detected performances of the device can be obtained, including response wavelength, dark current, photocurrent, and temperature dependence. A bias ranging from –5 V to +5 V was applied to evaluate the performance of the photodetector. The calculated current density was presented in the absolute form to indicate the trend of current density variation with voltage.

Based on the calculated current-voltage characteristics, the key detection parameters, including photocurrent density (J_{photo}), dark current density (J_{dark}), responsivity (R), photocurrent-to-dark-current ratio ($PDCR$), and detectivity (D^*), can be obtained as follows [26–29]:

$$R = \frac{J_{photo} - J_{dark}}{P} \tag{1}$$

$$PDCR = \frac{J_{photo}}{J_{dark}} \tag{2}$$

$$D^* = \frac{R}{\sqrt{2qJ_{dark}}} \tag{3}$$

Where P and q denote the incident optical power density and electron charge, respectively. By evaluating these parameters, the behavior of the Ga_2O_3 photodetector can be understood, thereby guiding further structural and performance optimizations.

3. Results and discussion

3.1. Influence of illumination wavelength and intensity

The performances of the MSM-structured Ga_2O_3 photodetector were calculated under various illumination conditions. Several representative monochromatic wavelengths were selected to comprehensively characterize the device's spectral response, covering solar-blind ultraviolet (254 nm), mid-ultraviolet (300 nm), near-ultraviolet (360 nm), visible (600 nm), and infrared (1200 nm) regions. This broad spectral range enables a thorough evaluation of the photodetector's performance across different photon energies.

Fig. 2 provides the current density-voltage (J-V) curves of the device under both dark conditions and monochromatic illumination at various wavelengths. The dark current J-V curve exhibits negligible deviation from the curves obtained under illumination at 300 nm, 360 nm, 600

nm, and 1200 nm. In contrast, under 254 nm illumination, the photocurrent density demonstrates a substantial enhancement compared to the dark current density. This result confirms that the MSM-structured Ga_2O_3 photodetector only demonstrates notable photoresponse in the short-wave ultraviolet spectral range, meeting the requirements for an ultraviolet photodetector. The bandgap of Ga_2O_3 of 4.8 eV corresponds to an absorption edge located at around 258 nm. When the photon energy of the incident light is equal to or larger than the bandgap of Ga_2O_3, electrons in the valence band can be excited to transition into the conduction band, thereby generating significant photo-generated carriers and subsequently leading to a noticeable increase in current density. In contrast, photon energies below 4.8 eV are insufficient to excite electrons across the wide bandgap of Ga_2O_3. Consequently, only 254 nm illumination generates the observed photoresponse in Fig. 2.

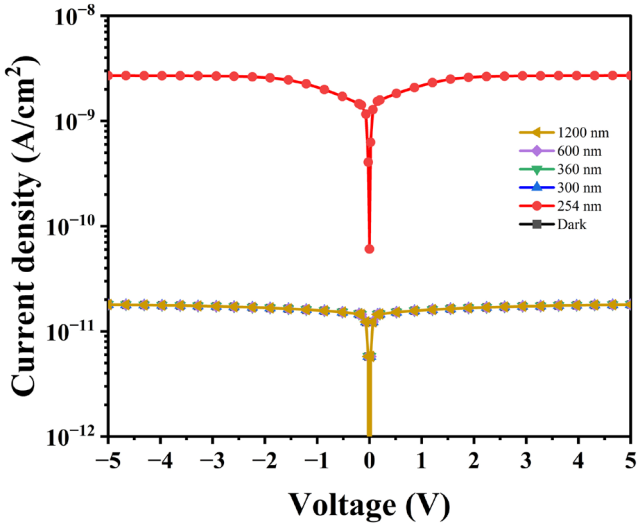

Fig. 2. Comparative analysis of the J-V characteristics for the Ga_2O_3 device under illumination at various wavelengths.

Figure 3 presents the *J-V* characteristics of a Ga_2O_3 photodetector illuminated with 254 nm light at varying intensities. The photocurrent density increases with the enhancement of illumination intensity due to the increasing photo-generated carriers. Fig. 4 presents the dependence of the detection parameters of the device on illumination intensity. The photocurrent density and photocurrent-to-dark-current ratio demonstrate a linear relationship with illumination intensity, whereas both responsivity and detectivity remain constant across the intensity range. This behavior confirms the photosensitivity and stability of the photodetectors.

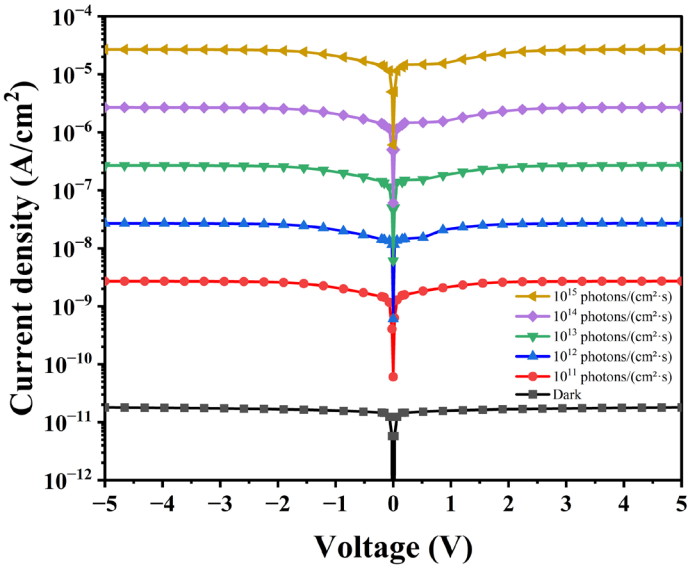

Fig. 3. J-V curves of the Ga_2O_3 device under 254 nm illumination with different intensities.

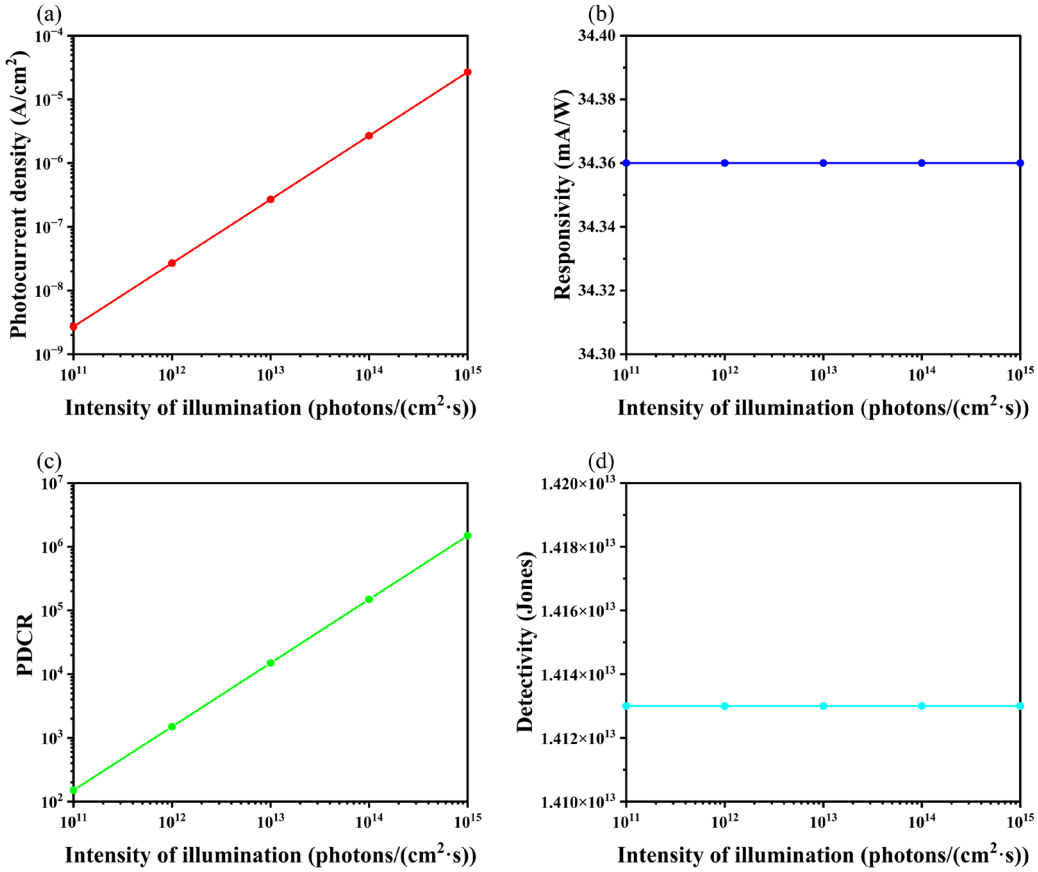

Fig. 4. Illumination intensity dependence of (a) photocurrent density, (b) responsivity, (c) photocurrent-to-dark-current ratio, and (d) detectivity for Ga_2O_3 photodetectors under +5 V bias.

To further explore the underlying physical mechanism, the internal energy band structure in the Ga_2O_3 photodetector is provided in Fig. 5. The interface between the front electrode and Ga_2O_3 is defined as the zero position, with the vacuum level at this interface serving as the zero

energy reference. Fig. 5(a) is the energy band diagram of the photodetector under thermal equilibrium. The n-type conductivity of Ga_2O_3 makes its Fermi level near the conduction band bottom. Since the work function of metal exceeds that of Ga_2O_3, a Schottky contact forms at the interface between metal and Ga_2O_3. The conduction band minimum and the valence band maximum in Ga_2O_3 bend upward to align with the vacuum energy level of the metal, forming a Schottky barrier. The majority of electrons in Ga_2O_3 need to overcome the upward bending barrier to flow into the metal, leading to a low dark current through the device. In Fig. 5(b), under 254 nm ultraviolet (UV) illumination, the Fermi level of Ga_2O_3 splits into electron and hole quasi-Fermi levels, indicating the absorption of ultraviolet light and formation of photo-generated carriers in the Ga_2O_3 layer.

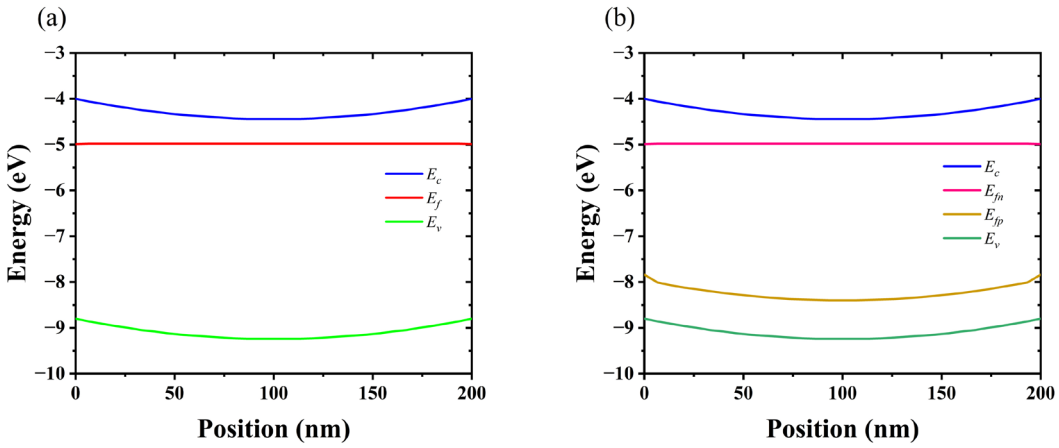

Fig. 5. Energy band diagrams of the Ga_2O_3 device under (a) dark conditions and (b) 254 nm illumination. E_c, E_f, E_v, E_{fn}, and E_{fp} denote the conduction band bottom, Fermi level, valence band top, electron quasi-Fermi level, and hole quasi-Fermi level, respectively.

Fig. 6 presents the spatial distribution of carrier density in the Ga_2O_3 photodetector under illumination. Under ultraviolet excitation, the electron concentration within the Ga_2O_3 layer increases by about two orders of magnitude compared to dark conditions. The electron concentration exhibits a decreasing trend from the central region of Ga_2O_3 toward both metal layers, which is consistent with the energy band structure in Fig. 5(b). The Schottky barriers at the Au/Ga_2O_3 interfaces suppress the injection of photo-generated electrons from Ga_2O_3 into the metal electrodes, resulting in lower electron concentrations at the interfaces. The hole concentration increases from an initial value of near zero at dark to approximately 8×10^4 cm^{-3} under illumination and shows a decreasing distribution toward metal, primarily attributed to the low hole mobility in Ga_2O_3.

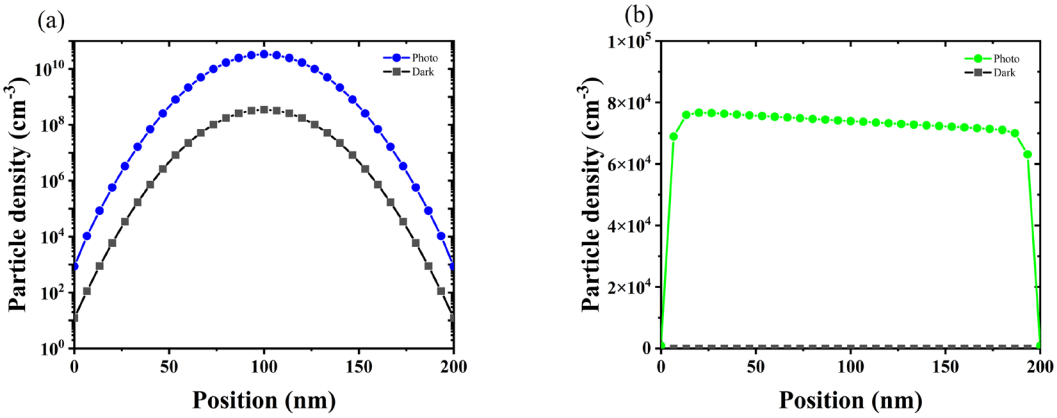

Fig. 6. Spatial distribution of photo-generated carriers in the Ga_2O_3 photodetector: (a) electron concentration and (b) hole concentration profiles before and after 254 nm illumination.

In the following section, the illumination condition is fixed at an intensity of 1×10^{11} photons/(cm^2·s) and a wavelength of 254 nm.

3.2. Influence of Ga_2O_3 thickness

Fig. 7 shows the comparison of dark and photo *J-V* curves for photodetectors with different Ga_2O_3 thicknesses. As the Ga_2O_3 thickness increases, the dark current density remains almost unchanged, whereas the photocurrent density demonstrates a consistent increasing trend.

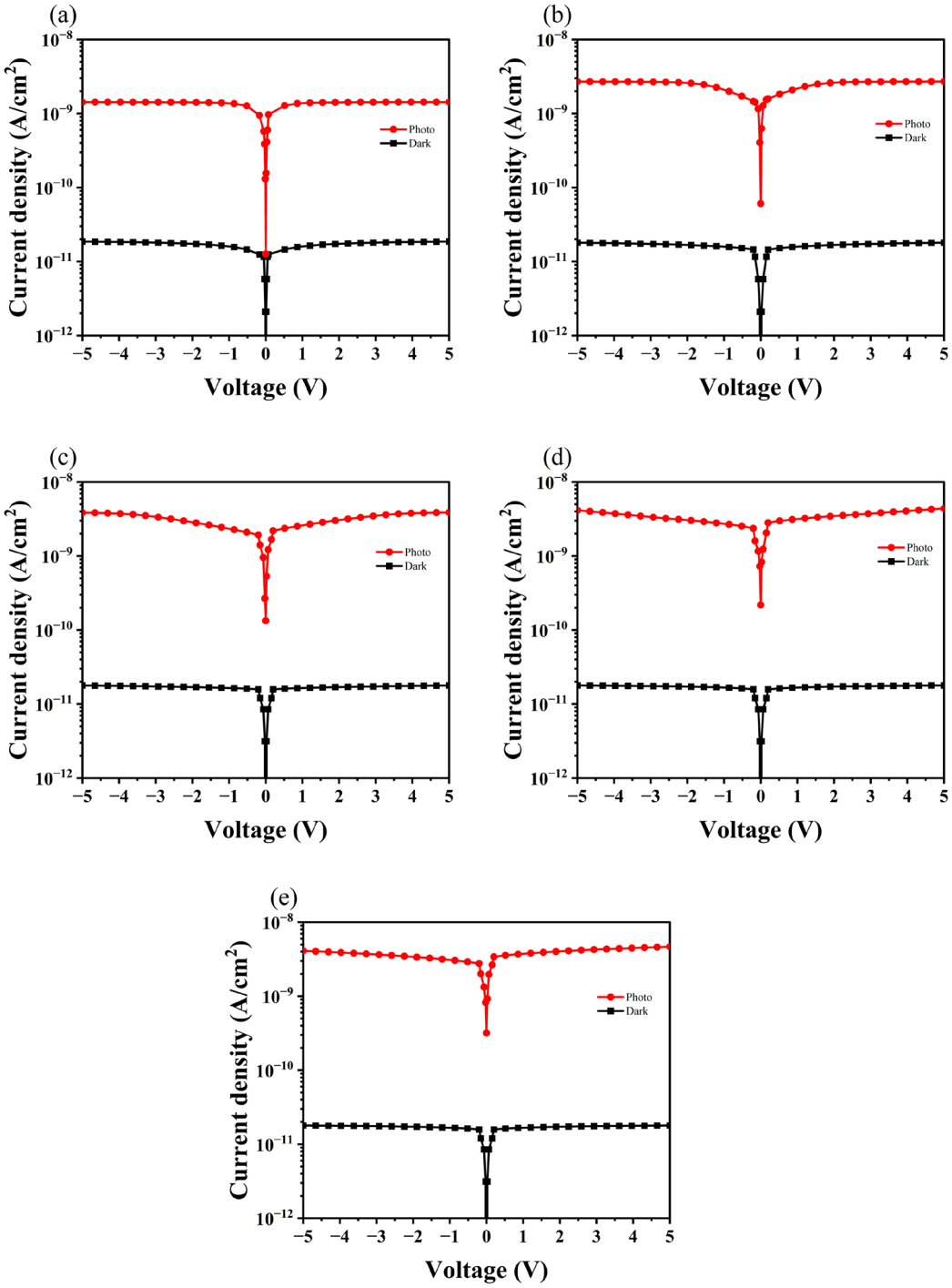

Fig. 7. Thickness-dependent J-V characteristics of Ga_2O_3 photodetectors with Ga_2O_3 thicknesses of (a) 100 nm, (b) 200 nm, (c) 300 nm, (d) 400 nm, and (e) 500 nm.

The influences of Ga_2O_3 thickness on the photocurrent density, dark current density, responsivity, photocurrent-to-dark-current ratio, and detectivity of the photodetector under +5 V bias were calculated and shown in Fig. 8. As the Ga_2O_3 thickness increases, the dark current density initially decreases until the thickness reaches 300 nm, after which it begins to increase. Conversely, the photocurrent density, responsivity, photocurrent-to-dark-current ratio, and detectivity all demonstrate a similar trend: rapid enhancement below 300 nm followed by slower

improvement at greater thicknesses. These findings indicate that an appropriate increase in Ga_2O_3 thickness contributes to the enhancement of the detection performance of the Ga_2O_3 photodetectors.

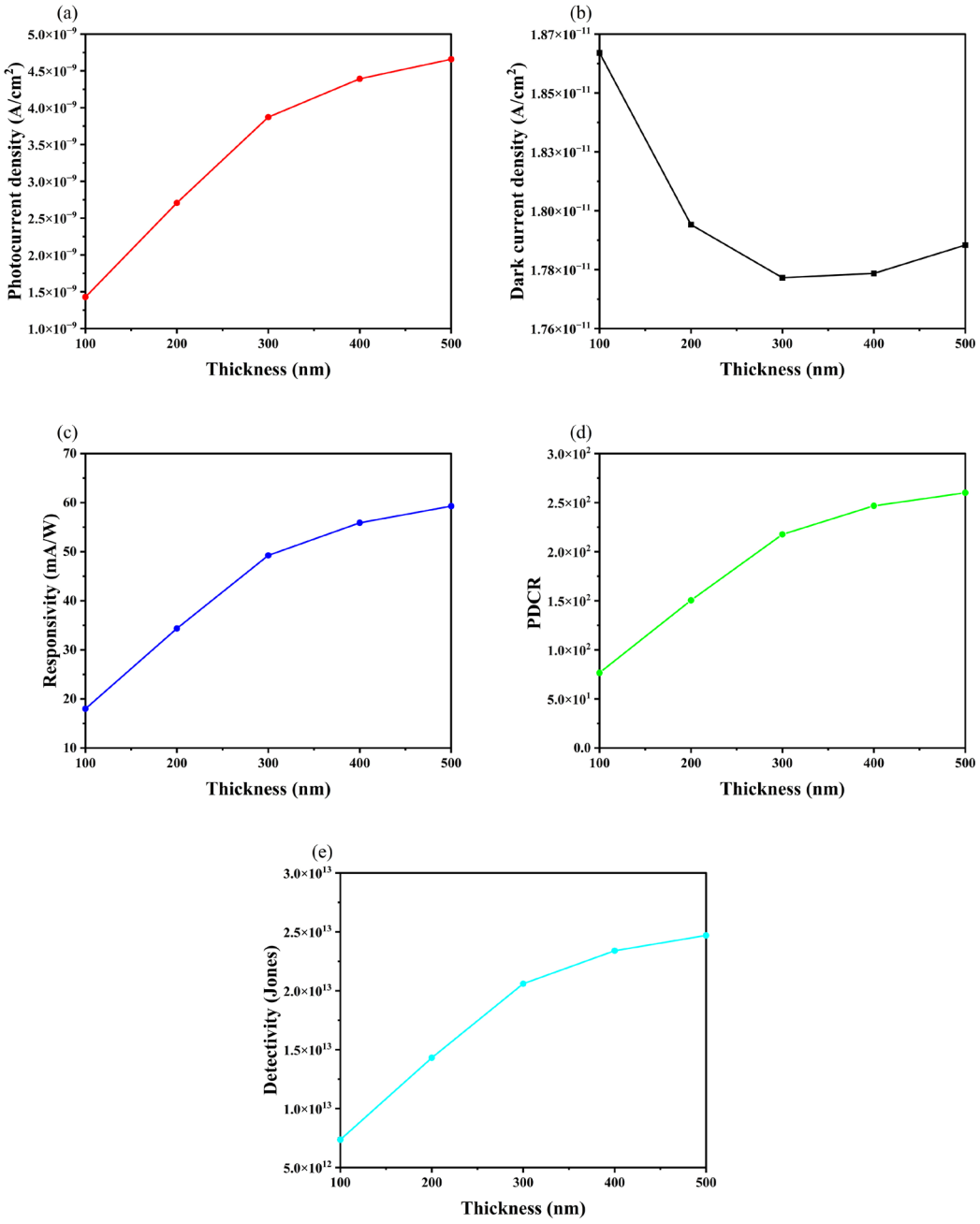

Fig. 8. Thickness dependence of (a) photocurrent density, (b) dark current density, (c) responsivity, (d) photocurrent-to-dark-current ratio, and (e) detectivity for Ga_2O_3 photodetectors under +5 V bias.

The effect of Ga_2O_3 thickness can be explained by the carrier generation and transport process. More ultraviolet photons are absorbed within the Ga_2O_3 layer as the thickness increases, leading to the more photo-generated electrons and holes, which result in the enhancements in photocurrent density and responsivity. On the other hand, as the Ga_2O_3 layer thickness increases, the transport path length for photo-generated carriers from their generation sites to the electrodes

extends, thereby enhancing the probability of carrier recombination within the device. Notably, under a fixed bias voltage, the applied electric field weakens with increasing Ga_2O_3 thickness, which further promotes carrier recombination. Consequently, the device's photodetection performance tends to saturate when the Ga_2O_3 thickness exceeds 300 nm.

The calculated results exhibit consistency with the thickness-dependent trend reported in the literature [30]. It was observed that the performance of the Ga_2O_3 photodetector demonstrated a rapid enhancement when the thickness increased from 210 nm to 840 nm, and tended to reach saturation when the thickness surpassed 840 nm [30].

3.3. Influence of the doping concentration of Ga_2O_3

Figure 9 shows the dark and photo *J-V* curves for Ga_2O_3 photodetectors with different doping concentrations of the Ga_2O_3 layer. The effects of the doping concentration of Ga_2O_3 layer on the detection parameters of Ga_2O_3 photodetector are presented in Fig. 10. The dark current density increases monotonously with the doping concentrations of Ga_2O_3 due to the increase amount of electrons and reduced resistivity of the Ga_2O_3 layer by doping. For the doping concentration below 5×10^{16} cm^{-3}, the photocurrent density and responsivity of the photodetector improve slightly. However, when the doping concentrations of Ga_2O_3 are higher than 5×10^{16} cm^{-3}, the photocurrent density, responsivity, photocurrent-to-dark-current ratio, and detectivity of Ga_2O_3 photodetector reduce rapidly because of the decrease of collection efficiency of photo-generated carriers induced by more non-radiative recombination centers and the enhanced carrier scattering. Therefore, an optimal doping concentration of Ga_2O_3 exists for achieving maximum detection performance.

Consistent with our findings, Ref. [31] reported a non-monotonic dependence of responsivity on Sn doping concentration in Ga_2O_3 photodetectors, where the responsivity initially increased before decreasing with higher doping levels. The study achieved a peak responsivity of 164 mA/W.

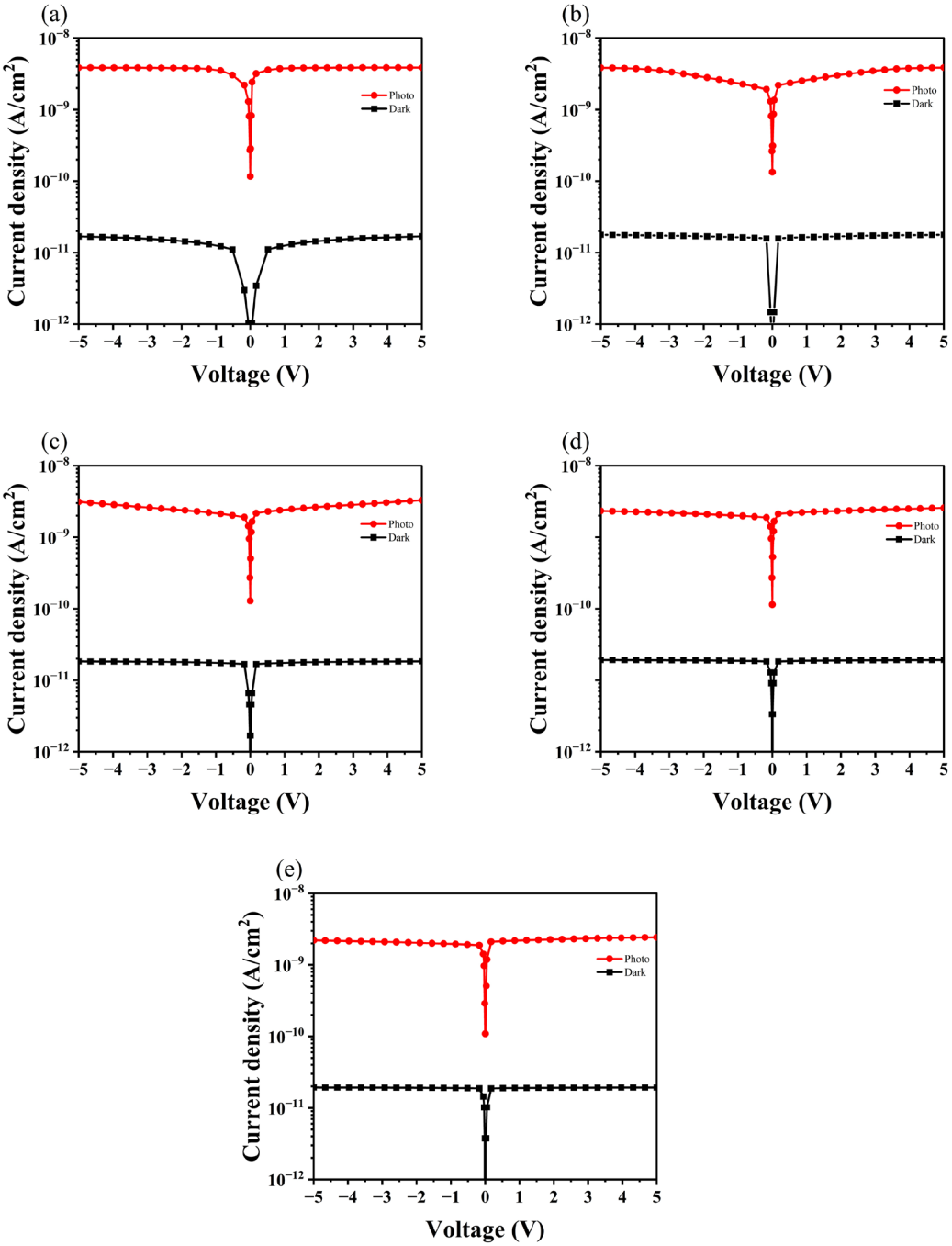

Fig. 9. J-V curves of Ga_2O_3 photodetectors with doping concentrations of (a) 1×10^{16} cm^{-3}, (b) 5×10^{16} cm^{-3}, (c) 1×10^{17} cm^{-3}, (d) 5×10^{17} cm^{-3}, and (e) 1×10^{18} cm^{-3}.

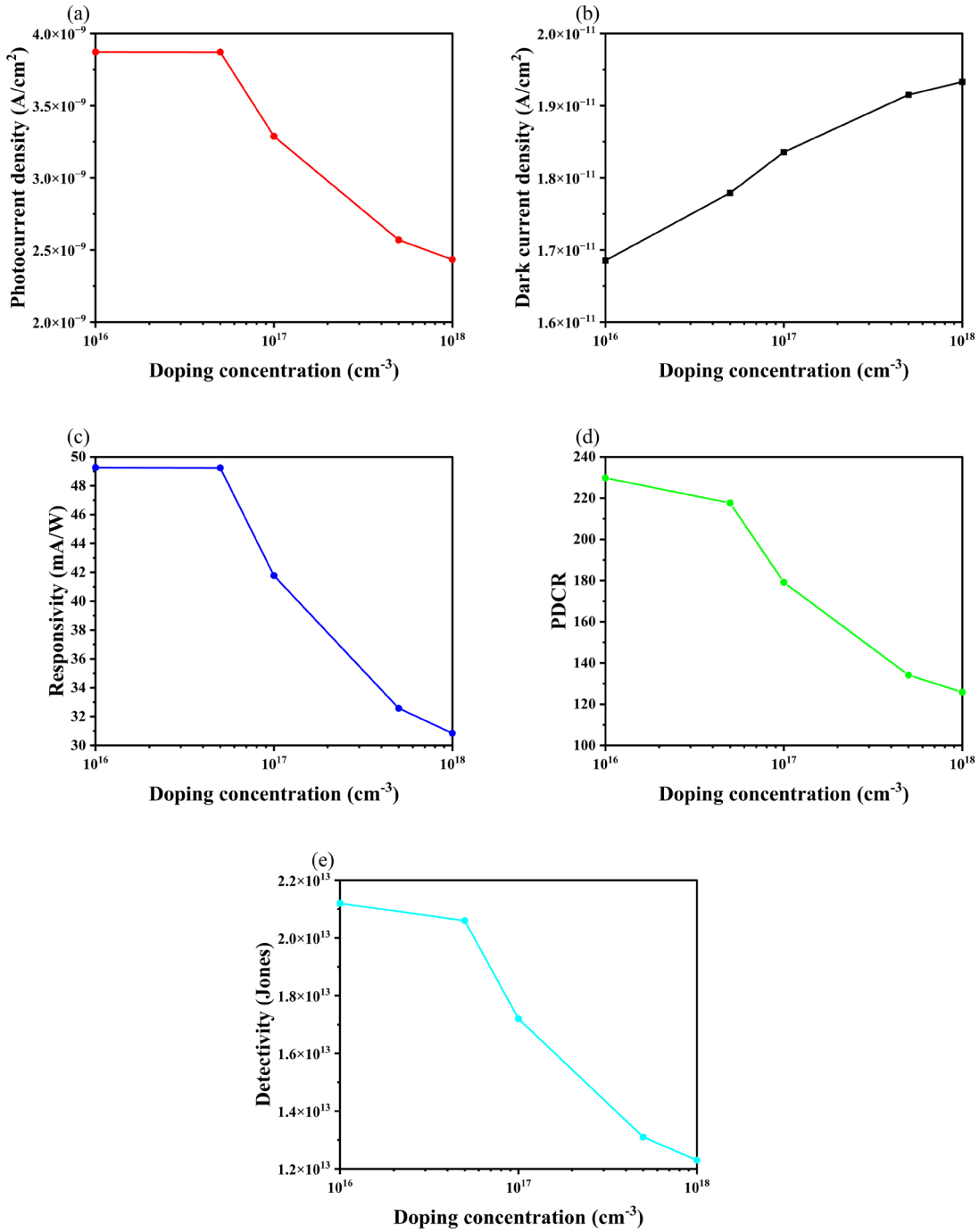

Fig. 10. Doping concentration dependence of (a) photocurrent density, (b) dark current density, (c) responsivity, (d) photocurrent-to-dark-current ratio, and (e) detectivity for Ga_2O_3 photodetectors under +5 V bias.

3.4. Influence of the operating temperature

The dark and photo *J-V* curves of the Ga_2O_3 photodetector at operating temperatures ranging from 240 K to 360 K are provided in Fig. 11. With increasing operating temperature, the dark current density increases significantly and approaches the level of photocurrent, which results from the intrinsic excitation effect induced by elevated temperatures. The intrinsic excitation of electrons from the valence band to the conduction band is enhanced at higher temperatures,

generating additional free carriers. Therefore, the carrier concentration increases in the Ga_2O_3 layer and dark current density of device rises.

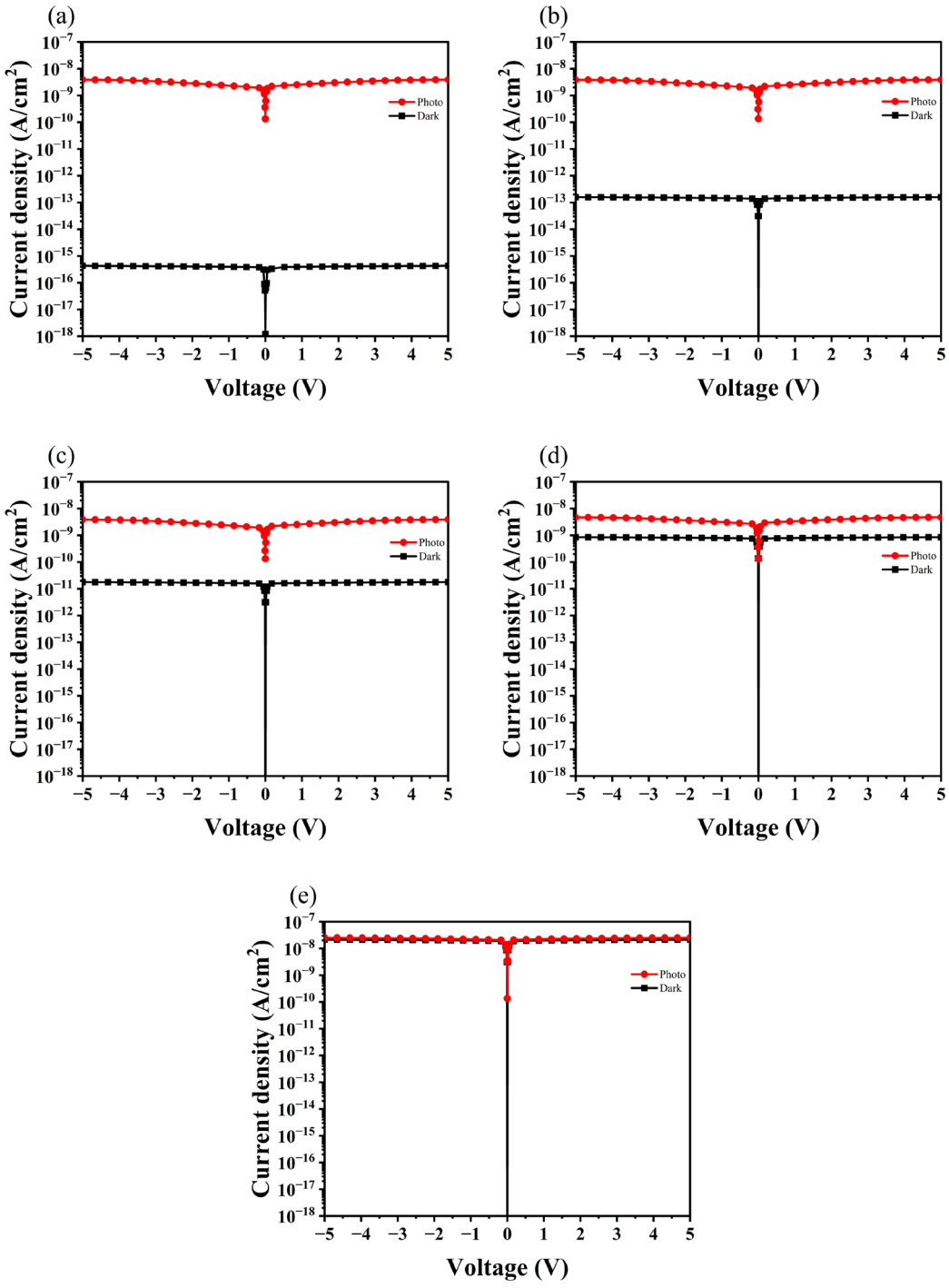

Fig. 11. Comparative J–V curves for Ga_2O_3 photodetectors operating at (a) 240 K, (b) 270 K, (c) 300 K, (d) 330 K, and (e) 360 K.

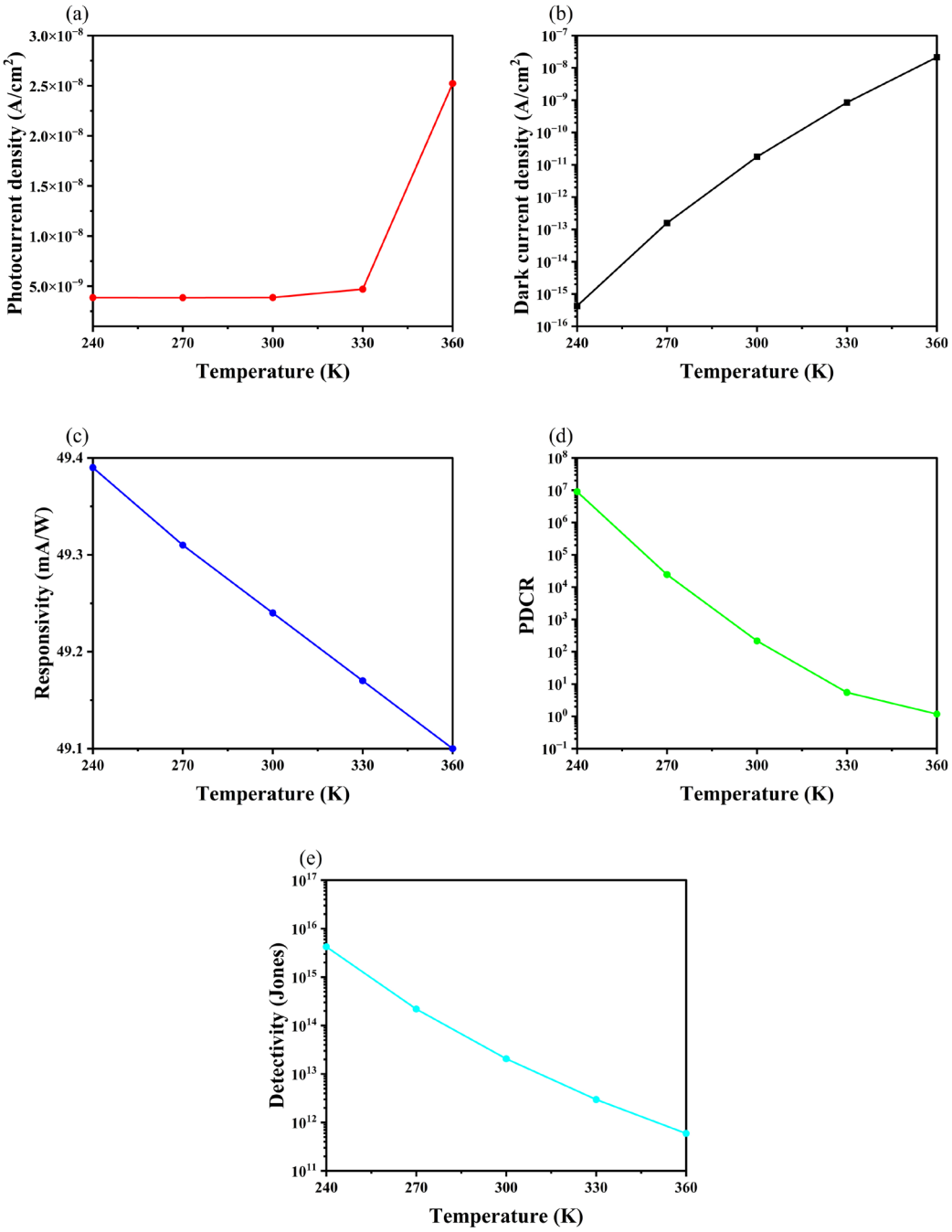

Fig. 12. Temperature dependence of (a) photocurrent density, (b) dark current density, (c) responsivity, (d) photocurrent-to-dark-current ratio, and (e) detectivity for Ga_2O_3 photodetectors under +5 V bias.

The changes of key performance parameters of Ga_2O_3 photodetector with operating temperature are further obtained according to the *J–V* curves and provided in Fig. 12. When the temperature is below 330 K, the photocurrent density remains nearly constant, indicating that the optical excitation mechanism is dominated and the concentration of photo-generated carriers is much higher than that of thermally excited carriers. However, when the temperature exceeds 330 K, the photocurrent density increases significantly, reflecting an enhancement of temperature-induced intrinsic excitation, which becomes the dominant carrier generation mechanism. At 360 K, the dark current density approaches the photocurrent density and the

photocurrent-to-dark-current ratio reduces to near 1, indicating that the thermally generated carriers has become dominated. The responsivity and detectivity of Ga_2O_3 photodetector decrease markedly with increasing operating temperature. Previous studies have demonstrated Ga_2O_3 device operation across a wide temperature range from 300 K to 800 K [32]. The results indicate that the dark current shows substantial enhancement with temperature, following an accelerated growth trend at elevated temperatures. The photocurrent increase remains comparatively modest. As a result, the rapid increase in dark current leads to a significant reduction in both photocurrent-to-dark-current ratio and detectivity at high temperature, which are consistent with the calculated results in this work.

The numerical calculations identify optimal device parameters as a thickness of 300 nm and a doping concentration of 5×10^{16} cm^{-3} in Ga_2O_3 layer, and operating temperature of 240 K. This configuration yields a dark current density of 4.26×10^{-16} A/cm^2, a responsivity of 49.39 mA/W, a photocurrent-to-dark-current ratio of 9.05×10^6, and a detectivity of 4.22×10^{15} Jones.

4. Conclusion

This study explored the performance of MSM-structured Ga_2O_3 solar-blind ultraviolet photodetectors under various device parameters and operational conditions by numerical method. The calculated results reveal that the semiconducting Ga_2O_3 absorbs photons in the solar-blind ultraviolet spectrum, inducing photo-generated electrons and holes and the quasi-Fermi level splitting. As the Ga_2O_3 layer is thickened, the absorption of ultraviolet light in the device improves, leading to an increase in photocurrent, photo-to-dark current ratio, responsivity, and detectivity and the enhancement tends to saturate beyond a thickness of 300 nm. The photocurrent density of the photodetector remains stable at Ga_2O_3 doping concentration below 5×10^{16} cm^{-3} but markedly decreases when the doping concentration exceeds this threshold. The reduced photocurrent at high doping amounts is attributed to the enhanced carrier recombination. The dark current density exhibits a gradual increase with rising doping concentration. Elevated operating temperatures induce a slight enhancement in photocurrent density but a sharp rise in dark current, causing rapid deteriorations in the photocurrent-to-dark-current ratio, responsivity and detectivity. The influence of temperature is attributed to the intrinsic excitation effect induced by high temperatures, weakening the device's detection performance. Therefore, suppressing dark current, especially in high-temperature environments, is crucial for improving the Ga_2O_3-based photodetectors. In this work, the MSM-structured Ga_2O_3 solar-blind ultraviolet photodetector demonstrates its optimal performance by a dark current density of 4.26×10^{-16} A/cm^2, a responsivity of 49.39 mA/W, a photocurrent-to-dark-current ratio of 9.05×10^6, and a detectivity of 4.22×10^{15} Jones. This study provides a deeper understanding of the conduction mechanisms in MSM-structured Ga_2O_3 photodetectors and guidelines for optimizing the structural design, material parameters, and operational condition control for high-quality Ga_2O_3 photodetectors.

Availability of Data and Materials

The datasets used and analyzed during the current study are available from the corresponding author on reasonable request.

Author Contributions

W. C. Huang and J. X. Xu designed the research study. W. C. Huang performed the research, analyzed the data, and wrote original draft of manuscript. J. X. Xu analyzed the data and edited the manuscript. Z. Liu provided supervision and advice on the calculations. All authors contributed to editorial changes in the manuscript. All authors read and approved the final manuscript. All authors have participated sufficiently in the work and agreed to be accountable for all aspects of the work.

Acknowledgements

Not applicable.

Funding

This research received no external funding.

Conflict of Interest

The authors declare no conflict of interest.

References

[1] J.J. Ding, P.F. Zhao, H.X. Chen, H.W. Fu, Appl. Phys. A **130,** 350 (2024); https://doi.org/10.1007/s00339-024-07501-y

[2] D. Kaur, M. Kumar, Adv. Opt. Mater. **9,** 2002160 (2021); https://doi.org/10.1002/adom.202002160

[3] L.J. Huang, Z.R. Hu, H. Zhang, Y.Q. Xiong, S.Q. Fan, C.Y. Kong, W.J. Li, L.J. Ye, H.L. Li, J. Mater. Chem. C **9,** 10354 (2021); https://doi.org/10.1039/D1TC02471J

[4] C.N. Lin, Y.J. Lu, Y.Z. Tian, C.J. Gao, M.M. Fan, X. Yang, L. Dong, C.X. Shan, Opt. Express **27,** 29962 (2019); https://doi.org/10.1364/OE.27.029962

[5] X.H. Chen, S.J. Huang, N. Nasiri, ACS Appl. Nano Mater. **7,** 3589 (2024); https://doi.org/10.1021/acsanm.3c04403

[6] K. Chen, Z.X. Li, Q. Liu, M.J. Xu, Q.L. Jiang, Z.X. Dong, X.F. Wang, X.M. Chen, S.T. Li, F.L. Gao, Appl. Phys. Lett. 124, 52103 (2024); https://doi.org/10.1063/5.0187137

[7] D.B. Li, K. Jiang, X.J. Sun, C.L. Guo, Adv. Opt. Photonics **10,** 43 (2018); https://doi.org/10.1364/AOP.10.000043

[8] Y. Yan, W.Q. Xiong, S.S. Li, K. Zhao, X.T. Wang, J. Su, X.H. Song, X.P. Li, S. Zhang, H. Yang, X.F. Liu, L. Jiang, T.Y. Zhai, C.X. Xia, J.B. Li, Z.M. Wei, Adv. Opt. Mater. **7,** 1900622 (2019); https://doi.org/10.1002/adom.201900622

[9] J.J. Xu, W. Zheng, F. Huang, J. Mater. Chem. C **7,** 8753 (2019);

https://doi.org/10.1039/C9TC02055A

[10] S.J. Pearton, J.C. Yang, P.H. Cary, F. Ren, J. Kim, M.J. Tadjer, M.A. Mastro, Appl. Phys. Rev. **5,** 11301 (2018); https://doi.org/10.1063/1.5006941

[11] A.S. Pratiyush, U. Ul Muazzam, S. Kumar, P. Vijayakumar, S. Ganesamoorthy, N. Subramanian, R. Muralidharan, D.N. Nath, IEEE Photonics Technol. Lett. **31,** 923 (2019); https://doi.org/10.1109/LPT.2019.2913286

[12] Z.N. Mao, J.X. Xu, Z.W. Tao, W.C. Huang, Y.X. Xu, Z. Liu, Phys. Status Solidi A **222,** 2400965 (2025); https://doi.org/10.1002/pssa.202400965

[13] K.L. Xia, Z. Liu, S. Li, G.R. Feng, Y.F. Guo, W.H. Tang, IEEE Photonics Technol. Lett. **36,** 143 (2024); https://doi.org/10.1109/LPT.2023.3330477

[14] C.G. Wang, J.T. Zhao, H.L. Cao, C. Shen, J. Tang, J. Liu, Opt. Express **31,** 33776 (2023); https://doi.org/10.1364/OE.495874

[15] K. Tang, L. Zhang, K.Y. Gu, H.F. Huang, Z. Liu, Z.L. Zhang, J. Huang, L.J. Wang, Mater. Today Phys. **42,** 101380 (2024); https://doi.org/10.1016/j.mtphys.2024.101380

[16] D. Kufer, G. Konstantatos, ACS Photonics **3,** 2197 (2016); https://doi.org/10.1021/acsphotonics.6b00391

[17] S.L. Kuang, Z.N. Yang, X.Y. Xu, Y.X. He, L.J. Bao, Z. Liang, K.K. Li, K. Ling, X. Zhang, Y. Yang, H. Long, Q.J. Cheng, X.Z. Liu, D.Y. Chen, H.J. Qi, K.H.L. Zhang, Adv. Opt. Mater. **13,** 2403049 (2025); https://doi.org/10.1002/adom.202403049

[18] C.Y. Huang, G.Y. Lin, Y.Y. Liu, F.Y. Chang, P.T. Lin, F.H. Hsu, Y.H. Peng, Z.L. Huang, T.Y. Lin, J.R. Gong, J. Vac. Sci. Technol. A **38,** 062409 (2020); https://doi.org/10.1116/6.0000512

[19] D.Z. Xu, P. Jin, P.F. Xu, M.Y. Feng, J. Wu, Z.G. Wang, Chin. Phys. B **32,** 108504 (2023); https://doi.org/10.1088/1674-1056/acc44d

[20] C.D. Zhang, F.F. Ren, M.B. Yu, B.S. Zhang, S.L. Gu, R. Zhang, Y.D. Zheng, J.D. Ye, J. Phys. D: Appl. Phys. **56,** 115102 (2023); https://doi.org/10.1088/1361-6463/acb36a

[21] R. Varache, C. Leendertz, M.E. Gueunier-Farret, J. Haschke, D. Muñoz, L. Korte, Sol. Energy Mater. Sol. Cells **141,** 14 (2015); https://doi.org/10.1016/j.solmat.2015.05.014

[22] M. Higashiwaki, K. Sasaki, A. Kuramata, T. Masui, S. Yamakoshi, Phys. Status Solidi A **211,** 21 (2014); https://doi.org/10.1002/pssa.201330197

[23] M.D. Zhu, B. Song, M. Qi, Z.Y. Hu, K. Nomoto, X.D. Yan, Y. Cao, W. Johnson, E. Kohn, D. Jena, H.G. Xing, IEEE Electron Device Lett. **36,** 375 (2015); https://doi.org/10.1109/LED.2015.2404309

[24] E.A. Jones, F. Wang, D. Costinett, IEEE J. Emerg. Sel. Top. Power Electron. **4,** 707 (2016); https://doi.org/10.1109/JESTPE.2016.2582685

[25] T. Goudon, V. Miljanović, C. Schmeiser, SIAM J. Appl. Math. **67,** 1183 (2007); https://doi.org/10.1137/060650751

[26] F. Wang, T. Zhang, R.Z. Xie, Z. Wang, W.D. Hu, Nat. Commun. **14,** 2224 (2023). https://doi.org/10.1038/s41467-023-37635-1

[27] X.R. Shu, J.F. Wu, F. Zhong, X.L. Zhang, Q. Fu, X. Han, J.L. Zhang, J.P. Lu, Z.H. Ni. Appl. Phys. Lett. **124,** 181101 (2024); https://doi.org/10.1063/5.0205803

[28] R.A. Yotter, D.M. Wilson, IEEE Sens. J. **3,** 288 (2003);

https://doi.org/10.1109/JSEN.2003.814651

[29] T.J. Ma, N. Xue, A. Muhammad, G. Fang, J.Y. Yan, R.K. Chen, J.H. Sun, X.G. Sun, Micromachines **15,** 1249 (2024); https://doi.org/10.3390/mi15101249

[30] X.H. Li, M. Zhang, J. Yang, S. Xing, Y. Gao, Y.Z. Li, S.Y. Li, C.J. Wang, Acta Phys. Sin. **71,** 048501 (2022); https://doi.org/10.7498/aps.71.20211744

[31] Y.N. Li, Y.Q. Li, Y. Ji, H. Wang, D.Y. Zhong, J. Mater. Sci. **57,** 1186 (2022); https://doi.org/10.1007/s10853-021-06680-w

[32] M.L. Zhang, W.Y. Ma, Z. Liu, L.L. Yang, S. Li, Y.F. Guo, W.H. Tang, Results Phys. **54,** 107110 (2023); https://doi.org/10.1016/j.rinp.2023.107110